AIAA JOURNAL
Vol. 43, No. 1, January 2005

Airfoil-Vortex Interaction Using the Compressible Vorticity Confinement Method

R. Morvant,* K. J. Badcock,† G. N. Barakos,‡ and B. E. Richards§
University of Glasgow, Glasgow, Scotland G12 8QQ, United Kingdom

The phenomenon of blade-vortex interaction (BVI) is central to the study of rotorcraft aerodynamics and aeroacoustics. The numerical simulation of BVI is challenging because most numerical schemes tend to alter the characteristics of the vortex, which must be preserved until the interaction. The compressible vorticity confinement method (CVCM) is capable of preserving vortices and requires minimal modifications to existing computational-fluid-dynamics codes. Inviscid and viscous calculations using a range of turbulence models have been carried out for a well-known, head-on BVI case. This is the first time CVCM is employed for turbulent flow calculations with an upwind solver. The results obtained using the CVCM show a good agreement with measurements.

Nomenclature

a	=	speed of the sound, ms^{-1}
C_p	=	surface-pressure coefficient
C_1	=	confinement parameter when the grid scaling is used
c	=	airfoil chord, m
$\boldsymbol{f}_b$	=	body force term, $\mathrm{kg\,m}^{-2}\mathrm{s}^{-2}$
$\boldsymbol{n}$	=	normalized vorticity gradient vector
p	=	pressure, Pa
R_c	=	viscous core radius, m
r	=	distance from the vortex core, m
S	=	source term of the vector form of the Navier–Stokes equations
U_∞	=	freestream velocity, ms^{-1}
$\boldsymbol{V}$	=	velocity vector, ms^{-1}
v_θ	=	tangential velocity, ms^{-1}
Γ	=	circulation, $\mathrm{m}^2\mathrm{s}^{-1}$
$\hat{\Gamma}$	=	normalized circulation
δ	=	density confinement parameter
ε	=	confinement parameter, ms^{-1}
μ	=	artificial dissipation coefficient, $\mathrm{kg\,m}^{-1}\mathrm{s}^{-1}$
ρ	=	density, $\mathrm{kg\,m}^{-3}$
ω	=	vorticity, s^1

I. Introduction

BLADE-VORTEX-INTERACTION (BVI) noise needs to be considered when simulating the acoustics of a helicopter because of its significant contribution to the perceived noise levels. BVI takes place both on the main and tail rotors with the vortex axis being parallel or orthogonal to the blades. The BVI noise is generated when the blade tip vortices collide or come close to the rotor blades.[1] As explained by Schmitz et al.,[2] the unsteady disturbances generated by the passage of a vortex close to a blade radiate a part of their energy as sound. Depending on the phase delay between the emitted acoustic waves, the BVI sound can propagate directionally and far from the rotor. It is therefore essential to understand the mechanisms of BVI because of its dominance on the acoustic signature of a helicopter, particularly in descending flight.[3,4]

In recent years, computational fluid dynamics (CFD) has made a significant impact in the design of modern rotors. Yet, the ability of most CFD codes to preserve vortices over long distances on grids of moderate density still remains questionable. This is mainly a result of the amount of numerical dissipation and dispersion inherent in most numerical schemes. The Parallel Multi-Block (PMB) code of the University of Glasgow[5] is used in the present work. This is a parallel, structured, multiblock code with implicit time stepping. It uses the Osher's and Roe's schemes and uses a preconditioned Krylov solver for efficiency.

To extend the capability of the code for predicting flows with strong vortical structures, the compressible vorticity confinement method (CVCM)[6–8] has been implemented. This method is particularly attractive because it is economic in terms of memory and CPU time and relatively simple to implement in existing solvers. This method has been successfully used for tracking vortices[9,10] and more specifically for rotorcraft simulations.[11] Application of the method is also reported for several other flow cases including flows over complex bodies,[12] massively separated flows,[13] and even flow visualization.[14] Recently, it was used for the simulation of blade-vortex interaction,[6] which is the main focus of this paper.

The well-known experiment of Lee and Bershader[15] provides the basis of the current work. This experiment concerns the head-on parallel BVI between a vortex and a NACA-0012 airfoil. Because detailed measurements of the surface pressure on the upper and lower sides of the blade are available for this experiment, this case has been previously used as a benchmark. Different techniques such as high-order schemes,[15,16] local grid refinement,[17] and more recently unstructured adaptive meshes[18,19] were used to preserve the convected vortex. The advantage of the CVCM is that it allows the use of relatively coarse grids along the vortex path and refined grids near the airfoil so that accurate predictions of the surface pressure and well-preserved near-field acoustical waves can be obtained.

The complex flowfield of the head-on BVI is known to produce a very intense impulsive noise.[15] As mentioned in Ref. 20, this noise has four main contributions: 1) from the vortex at subsonic speed with its upwash or downwash velocity component, 2) from the stall and reattachment of the flow when the vortex approaches the airfoil, 3) from the oscillation of the stagnation point as a result of the high-pressure region generated at the leading edge (LE) of the airfoil (compressibility waves), and 4) from the development of a supersonic area at the shoulder of the airfoil (transonic waves).

This paper will first illustrate the capabilities of the vorticity confinement method using a simple benchmark problem of vortex convection in an infinite domain. Once confidence in the method is established, the simulation of the head-on BVI will be attempted, and comparisons will be made between the CFD results and the

Received 13 September 2003; revision received 25 February 2004; accepted for publication 27 July 2004.

*Research Student, Computational Fluid Dynamics Laboratory, Department of Aerospace Engineering.

†Reader, Computational Fluid Dynamics Laboratory, Department of Aerospace Engineering.

‡Lecturer, Computational Fluid Dynamics Laboratory, Department of Aerospace Engineering.

§Mechan Professor, Computational Fluid Dynamics Laboratory, Department of Aerospace Engineering. Associate Fellow AIAA.

experiments of Lee and Bershader.[15] Parameters that are likely to influence the BVI results will be studied: vortex location, spatial and time refinement, and the influence of corrections to the angle of attack. Finally, the near-field acoustics of the NACA-0012 will be presented along with Mach-number effects.

II. Compressible Vorticity Confinement Method

A. Principle of the VCM

The vorticity confinement method (VCM) developed by Steinhoff et al.[7] is aimed at countering the dissipation of the numerical scheme employed in CFD. The VCM is based on the observation that the numerical scheme tends to dissipate the vortices in the flow. Therefore, the VCM adds a source of momentum to balance this in regions of the flowfield where vorticity is concentrated. The basic modification is to add a body force term $\boldsymbol{f}_b$ to the momentum transport equations, which for incompressible flow reads

$$\rho\frac{\partial \boldsymbol{V}}{\partial t}+\rho(\boldsymbol{V}\cdot\nabla)\boldsymbol{V}+\nabla p=\mu\nabla^2\boldsymbol{V}-\boldsymbol{f}_b \tag{1}$$

The body force term $\boldsymbol{f}_b$ is given by $\rho\varepsilon(\nabla|\boldsymbol{\omega}|/|\nabla|\boldsymbol{\omega}||)\times\boldsymbol{\omega}$.

B. Compressibility Modifications

The extension of the VCM to the compressible Euler's equations has been realized by including the work of the body source term in the energy equation.[21] The integral form of the Navier–Stokes equations can be rewritten for a two-dimensional problem as

$$\frac{\mathrm{d}}{\mathrm{d}t}\int_{\vartheta}W\,\mathrm{d}\vartheta+\int_{\Sigma}F\cdot\boldsymbol{n}\,\mathrm{d}\Sigma+\int_{\Sigma}G\cdot\boldsymbol{n}\,\mathrm{d}\Sigma=-\int_{\vartheta}S\,\mathrm{d}\vartheta \tag{2}$$

where the conservative variables W, the fluxes F, G and the source term S can be expressed as

$$W=\begin{Bmatrix}\rho\\ \rho u\\ \rho v\\ \rho e\end{Bmatrix},\qquad F=\begin{Bmatrix}\rho u\\ \rho u^2+p\\ \rho uv\\ \rho uh\end{Bmatrix},\qquad G=\begin{Bmatrix}\rho v\\ \rho uv\\ \rho v^2+p\\ \rho vh\end{Bmatrix}$$

$$S=\begin{Bmatrix}S_\rho\\ S_u\\ S_v\\ S_e\end{Bmatrix}=\begin{Bmatrix}0\\ \varepsilon\rho(\boldsymbol{n}\times\boldsymbol{\omega})\cdot\boldsymbol{i}\\ \varepsilon\rho(\boldsymbol{n}\times\boldsymbol{\omega})\cdot\boldsymbol{j}\\ \varepsilon\rho(\boldsymbol{n}\times\boldsymbol{\omega})\cdot\boldsymbol{V}\end{Bmatrix}\quad\text{with}\quad\begin{cases}\boldsymbol{n}=\dfrac{\nabla|\boldsymbol{\omega}|}{|\nabla|\boldsymbol{\omega}||}\\ \boldsymbol{\omega}=\dfrac{\partial}{\partial\boldsymbol{M}}\times\boldsymbol{V}\end{cases} \tag{3}$$

In the preceding, u, v, and w are the components of the velocity vector, h is the total enthalpy per unit mass, and Σ is the surface and ϑ the volume of each control cell. The term $-\rho\varepsilon(\nabla|\boldsymbol{\omega}|/|\nabla|\boldsymbol{\omega}||)\times\boldsymbol{\omega}$ is added to the transport equations of the momentum components. In the preceding, $\boldsymbol{n}$ is the normalized ratio of the vorticity gradient amplitude. To include the work done by the body source term in the energy conservation law, the term $-\varepsilon\rho(\boldsymbol{n}\times\boldsymbol{\omega})$ also contributes as a part of the residual. A complete review of the compressible vorticity confinement method is given in the thesis by Hu.[22]

C. Implementation

The vorticity gradient is required for the source term S. The derivatives were calculated from their curvilinear form. It was found that the performance of the method depends strongly on the order of accuracy of the calculated gradients. Therefore the derivatives f_i' were estimated using fourth-order finite differences from

$$f_i'=\frac{-f_{i+2}+8f_{i+1}-8f_{i-1}+f_{i-2}}{12} \tag{4}$$

The use of high-order derivatives provides a better estimation of the vorticity gradients particularly in the wake of the airfoil. In addition, Laplacian smoothing to the vorticity and its gradient was applied. Regarding the temporal treatment, the Jacobians in the implicit formulation were left unchanged. Experience with the test cases presented in this paper (see Sec. IV.E) has shown that the stability and convergence of the scheme were not affected by the CVCM.

D. Modifications to the Basic Method

Different methods have been used to set the values for the parameters ε and μ:

1) Parameters ε and μ are set to constants. The constant ε and μ were respectively chosen so as to control the amount of momentum injected into the flow and to remove any excessive momentum that might create artificial vortices. The value of ε ranges typically from 0.001 to 0.1, whereas the parameter μ was set to a value between 0.1 to 1.0.

2) Use a vorticity-gradient-based limiter. It has been attempted to reduce the production of spurious vortices via the use of a limiter based on the vorticity gradient. Indeed, it was observed that some of the secondary vortices stem from the vector $\boldsymbol{n}$. The cross product of the vector $\boldsymbol{n}$ and the vorticity $\boldsymbol{\omega}$ allows the concentration of the antidissipation term in the areas where the magnitude of the vector $\boldsymbol{n}$ is significant. However, the vector $\boldsymbol{n}$ can have a large magnitude even in areas of low vorticity, and this can result in artificial vortices. Therefore, the vorticity ω was set to zero when the magnitude of the vorticity gradient $|\nabla|\boldsymbol{\omega}||$ was low.

3) Use a parameter ϵ scaled with the grid. Because the confinement parameter ϵ is homogeneous to the velocity, it is possible to scale it with the grid size and several formulations have been proposed.[9,23,24] The formulation proposed in Ref. 9. expresses the confinement parameter as $\varepsilon=h^2|\nabla|\boldsymbol{\omega}||$ with h the characteristic length that is equal to the scalar product of the cell size vector $\boldsymbol{L}=(\Delta x,\Delta y,\Delta z)$ with the vector $\boldsymbol{n}$. This formulation has been tested and compared against the constant scaling ε. Results are shown in Sec. III.

4) The density confinement method was proposed by Costes and Kowani.[23] It consists of adding a source term to the continuity equation. The source term S [see Eq. (3)] has a component S_ρ, which can be expressed as

$$S_\rho=\delta\frac{1}{|\boldsymbol{\omega}|}\left(S_u\frac{\partial\rho}{\partial x}+S_v\frac{\partial\rho}{\partial y}\right) \tag{5}$$

The nondimensionalized parameter δ allows the modification of the density in the vortex.

III. Evaluation of CVCM on a Vortex Convection Test Case

The CVCM was first tested on the benchmark problem of vortex convection in an infinite domain. An isentropic vortex was introduced into the flow and convected at the freestream velocity. Periodic boundary conditions were applied to enable the vortex to convect for many cycles. The Scully model was chosen because of its wide acceptance in the literature.[15] According to this model, the expression for the tangential velocity component is

$$v_\theta/U_\infty=(\hat{\Gamma}/2\pi r)\left[r^2\Big/\left(r^2+R_c^2\right)\right] \tag{6}$$

with U_∞, $\hat{\Gamma}$, R_c being, respectively, the freestream velocity, the nondimensionalized circulation, and the core radius. The nondimensionalized circulation $\hat{\Gamma}$ is equal to $\Gamma/(U_\infty c)$, c being the chord. Note that the pressure and density are calculated from the approximation of the Euler equations $\mathrm{d}p/\mathrm{d}r=\rho(v_\theta^2/r)$ and the isentropic relation $p=a\rho^\gamma$ (Ref. 22).

The influence of the confinement parameter and of the dissipation term is examined for the case $R_c=0.018$, $\hat{\Gamma}=-0.283$, and $M=0.5$. The calculations were carried out on two uniform grids: a coarse grid with 51×102 points and a finer grid of 139×278. Different values for the confinement coefficient ε have been used, the dissipation coefficient μ being set to zero. The flow was first considered as laminar with a Reynolds number based on the width of the domain of 1000. The grid extends from -0.5 to 0.5 in the X direction and from -1.0 to 1.0 in the Y direction. Figure 1 shows that the ω/ρ ratio is maintained constant when the CVCM is used while it is significantly reduced when $\varepsilon=0$. The method leads to the formation of artificial secondary vortices when the dissipation coefficient μ is set to zero. The dissipation term reduces the creation of artificial vortices and results in better preservation of the shape of the original vortex.

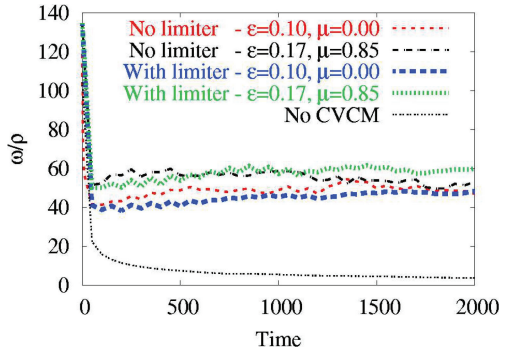

Fig. 1 Time history of the ω/ρ ratio at the vortex core as predicted using the CVCM method with or without gradient-based vorticity limiters.

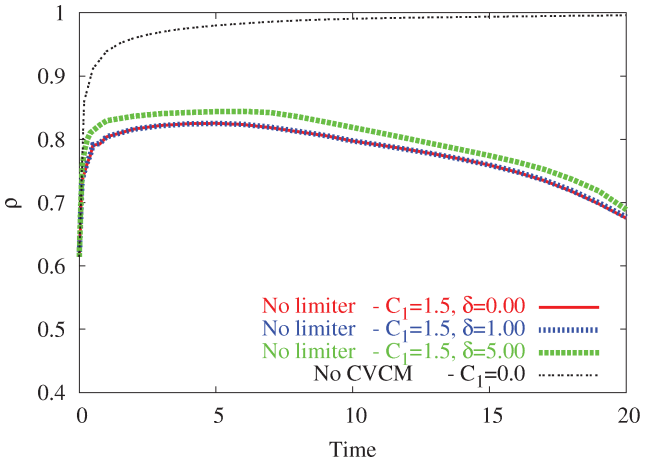

Fig. 2 Time history of the density at the vortex core using the density confinement.

Results with the use of the vorticity-gradient-based limiter show that the shape of the vortex is better preserved, even when the artificial dissipation coefficient μ is set to zero. Therefore, the only parameter remaining was the confinement term ε.

The density confinement method (method 4) was tested with the use of the grid scaling (method 3). The influence of the δ parameter was evaluated on a coarse grid. Figure 2 presents the history of the density at the vortex core for different values of δ with the density confinement. As can be seen, without CVCM the density increases at the vortex core, which is not realistic (an increase of the density means a weaker vortex). The solution without the density confinement ($\delta = 0.0$) is close to what can be obtained when the density confinement is applied. However, a closer look at the vortex core (Fig. 3) reveals that the density confinement allows a better preservation of the flow region near the eye of the vortex. This is in agreement with the observations of Costes and Kowani.[23] Regarding the vortex shape preservation, it seemed that a parameter δ set to 5.0 was the best option.

The use of the CVCM allows the tracking of the vortex for several cycles. On the coarse grid, the vortex is well-preserved even after 20 cycles, whereas it disappears after only two cycles without CVCM. On the fine grid and without CVCM, the vortex is five times weaker in terms of the ω/ρ ratio at the vortex core after 20 cycles of convection. The combination of methods 2 and 3 gives the best results for preserving the vortex characteristics and was therefore preferred to method 1. Note that the CPU time incurred by the use of the CVCM is minimal.

IV. Optimization of the BVI Simulation Using the CVCM

An airfoil test case is now considered in order to determine the optimum parameters for simulating BVI. The test case here is the

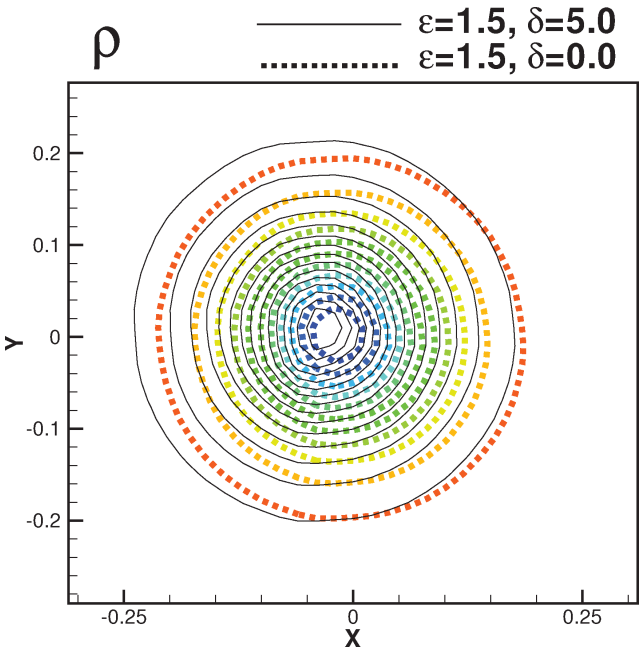

Fig. 3 Density contours obtained using the the density confinement. Note that the vorticity gradient limiter is not used.

parallel BVI between a clockwise vortex and a NACA-0012 airfoil. The nondimensionalized radius of the vortex R_c/c and its circulation $\Gamma/(U_\infty c)$ are set, respectively, to 0.018 and -0.283 as for the benchmark problem. Both inviscid and viscous calculations were carried out. Results will be shown for the head-on BVI at freestream Mach numbers of 0.5 and of 0.8.

A. Characteristics and Behavior of the CVCM for the BVI Simulation

The simulation of BVI requires the use of nonuniform grids. The scaling with the cell size was therefore combined with the vorticity gradient limiter for this study. Although it is suspected that the use of the density confinement will be useful if the vortex is to be well captured for long distances, the use of the vorticity gradient limiter for the confinement parameter was preferred for our study, the ε term remaining the only parameter of the CVCM. A comparison between the methods is given in Sec. IV.B for the BVI problem.

The grid used for the BVI simulation was carefully generated so that spacing along the expected path of the vortex is as uniform as possible. Moreover, the CVCM was not needed near the airfoil because the grid was fine enough in this area to capture the vortices. In addition, some robustness problems arose when running the calculations for values of ε, which are too large. Indeed, the employed CVCM formulation was found to modify the boundary layer and to amplify the wake, which is characterized by a large value of vorticity. One approach is to circumvent this problem by using the surface confinement method.[25] In this work, however, zones are used to restrict the effect of the source term to vortices avoiding wakes and boundary layers: the confinement method was not applied up to a distance 0.1 chords from the airfoil and also when the vorticity gradient exceeded a cutoff value. No confinement was applied near the airfoil, and so the CVCM does not alter the behavior of the turbulence models during the interaction. Note that the optimum ε parameter was found to depend on the Roe's and Osher's spatial schemes used, of which dissipation properties vary with the grid cell length, the time step, and the nature of the flow.

The importance of different parameters has also been evaluated: vortex location, spatial and time refinement, and angle of attack. Inviscid and viscous calculations have been attempted, and the freestream Reynolds number, based on the chord, was set to 10^6 for the viscous case, within the range of values 0.9×10^6–1.3×10^6 given for the experiments. The viscous calculations were expected to predict better the surface-pressure coefficient on the lower part

of the airfoil. As will be shown, it is essential to include the viscous effects because they affect the transfer of energy between vortices as well as between a vortex and the boundary-layer flow as mentioned by Körber and Ballmann in Ref. 26. The best parameters for simulating BVI can be determined by examining the results obtained for the low-speed case (freestream Mach number 0.5). The selected set of parameters was kept constant for the head-on BVI at a freestream Mach number of 0.8.

B. Influence of the CVCM

Inviscid and viscous calculations were carried out for different values of ε for a vortex introduced 4.5 chords ahead of the airfoil. The k–ω model was chosen for the viscous calculations. As shown in Fig. 4, the surface-pressure coefficient is well predicted for both inviscid and viscous calculations assuming the optimum value of ε is chosen, whereas they are very much underestimated when no CVCM is applied.

The importance of the ε parameter, which determines how the vortex is preserved, is now highlighted. Figure 5 presents density contours around the vortex before the interaction. The value of the density at the vortex core is expected to be around 0.6. It appears that the vortex strength increases with ε for the inviscid calculations. Too high a value of ε leads to a nonphysical flow, and too low a value does not allow the preservation of the vortex. The good prediction of the C_p history shows that the CVCM that uses the ε scaled with the grid and the vorticity gradient limiter is able to preserve the vortex characteristics for inviscid calculations.

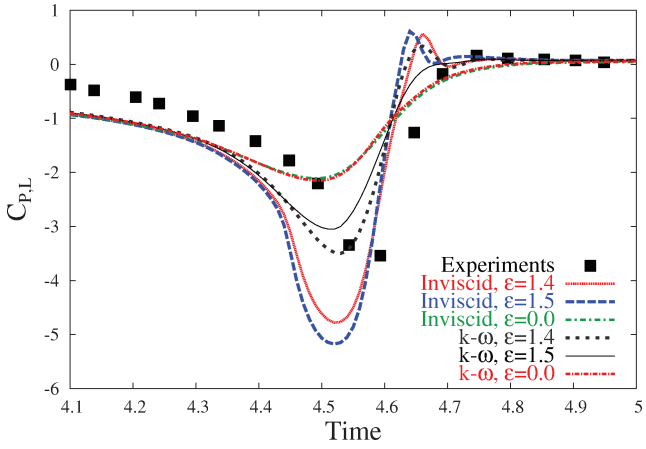

a) Lower surface, $x/c = 0.02$

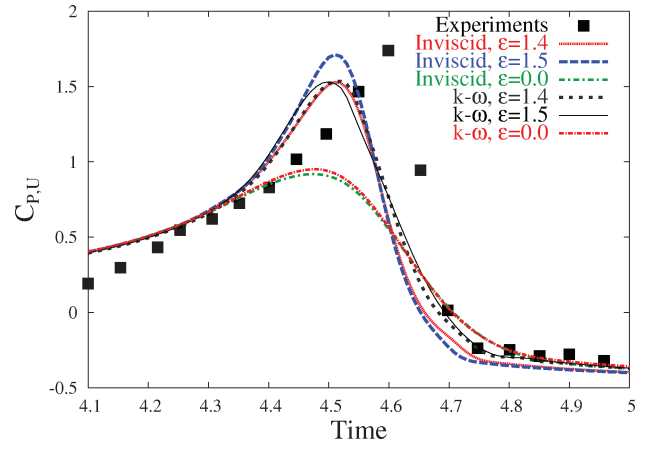

b) Upper surface, $x/c = 0.02$

Fig. 4 Influence of the value of the confinement parameter ε on the time history of the surface-pressure coefficient for inviscid and viscous calculations. The vortex was introduced at 4.5 chords ahead of the airfoil. Head-on BVI problem, NACA-0012 airfoil, Mach number 0.5, $x/c = 0.02$.

Regarding viscous calculations, too high a value of ε also makes the vortex too strong as depicted in Fig. 5. However, the best prediction of the C_p history was not obtained for $\varepsilon = 1.5$ as was the case for the inviscid calculations but for a value of 1.4. For this case, the dimensionless value of density was 0.62 at the vortex core, which is close to the desired 0.6. For $\varepsilon = 1.6$, a much lower value was obtained as can be seen from the legend of Fig. 5. The vortex core radius was found to change with the value of ε and the employed turbulence model. This is discussed in more detail in Sec. IV.G.

It was also investigated whether the vorticity gradient limiter coupled with the density confinement (methods 2 and 4) could help in obtaining a better match with the experiments for viscous calculations when ε is equal to 1.5. Despite the fact that the surface-pressure coefficient on the upper surface was better predicted with this method (2–4), the values of C_p on the lower surface remained underpredicted. Then, viscous calculations using the density confinement have been run for a parameter of 1.4, which gave the best results with the use of the vorticity gradient limiter. The use of the density confinement gave similar results for this test case. As expected, the Mach number has an influence on the ε parameter, and, in this work, a value of 1.4 was used for the subsonic case. A slightly higher value of 1.8 was found to be necessary for transonic cases.

C. Influence of the Initial Vortex Location

The initial vortex location is important because the Scully vortex needs to be introduced in a potential-like flow region. Different locations have been tested to check whether the history of the pressure coefficient changes and also whether the vortex is preserved in a similar way for different initial locations. Four locations have been used, namely, 1.5, 2.5, 3.5, and 4.5 chords ahead of the airfoil, and results are shown in Fig. 6. All calculations shown are inviscid, and a grid of approximately 500 thousand cells has been used. The results using the CVCM compare very well against the experiments for the four vortex locations. The pressure coefficients are well predicted, whereas they are very much underestimated when no CVCM is applied.

The k–ω model was used for viscous calculations. It was found that the peak of surface-pressure coefficient was not of the same magnitude for various vortex locations and for a fixed ε parameter. The vortex core radius, which should be of the same size as for the inviscid calculations, appeared to vary depending on the value of ε. It seems that the dynamics of the vortex, which is related to the turbulence model and to the CVCM, is at the origin of such differences. This is discussed in more detail in Sec. IV.G. Nevertheless, as for the inviscid calculations it will be shown in the next section that the trace of the interaction on the C_p is in good agreement with the experiments, whereas it is very weak when no confinement is used.

D. Influence of the Spatial Refinement

Two grids of different density along the vortex path have been used for the inviscid runs: a coarse grid of 125,000 points and a fine grid of 485,000 points. The coarse and fine grids have respectively two and four cells across the core radius, corresponding to a grid density similar to the one used in the benchmark problem. The ε parameters for the coarse and fine grids were respectively set to 1.5 and 0.5. Again, the C_p is well predicted on both grids (Fig. 7). It was found that the good agreement depends on the choice of the ε parameter. Knowing the optimum ε value for a particular grid density, it is possible to estimate the ε value on another uniform grid by simply assuming it is inversely proportional to the cell area.

Viscous calculations were run on two grids for the k–ω model: a coarse grid of 220,000 points and a fine grid of 820,000 points. Results are similar on both grids for the main interaction as shown in Fig. 8. Better agreement against the experiments is obtained for viscous calculations, especially for the pressure coefficient at the lower surface (see Fig. 6). This is expected as viscosity makes the encounter less impulsive.[27] In fact, viscous calculations can

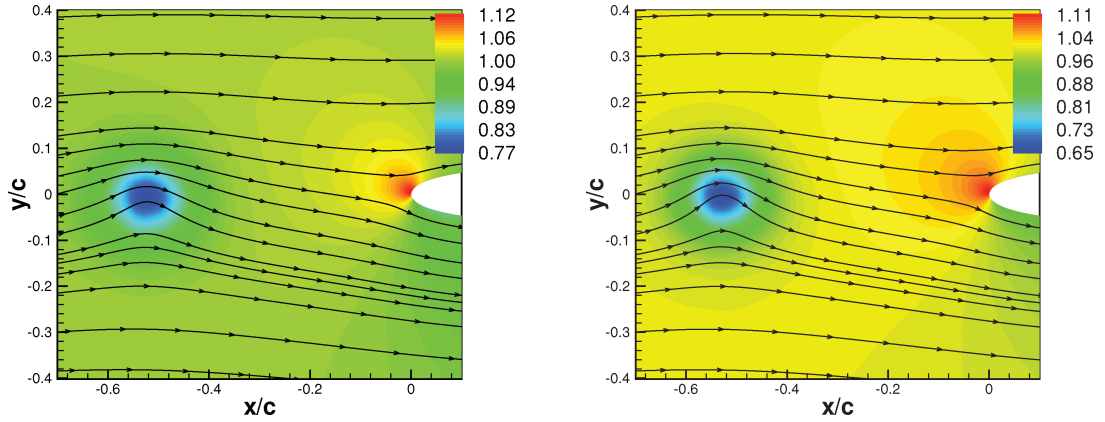

a) $\varepsilon = 1.4$: Inviscid

d) $\varepsilon = 1.4$: Viscous

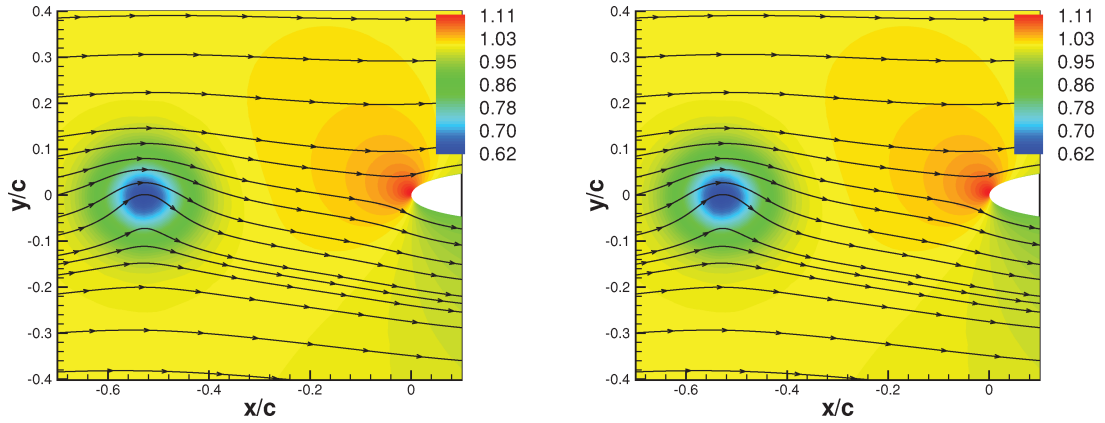

b) $\varepsilon = 1.5$: Inviscid

e) $\varepsilon = 1.5$: Viscous

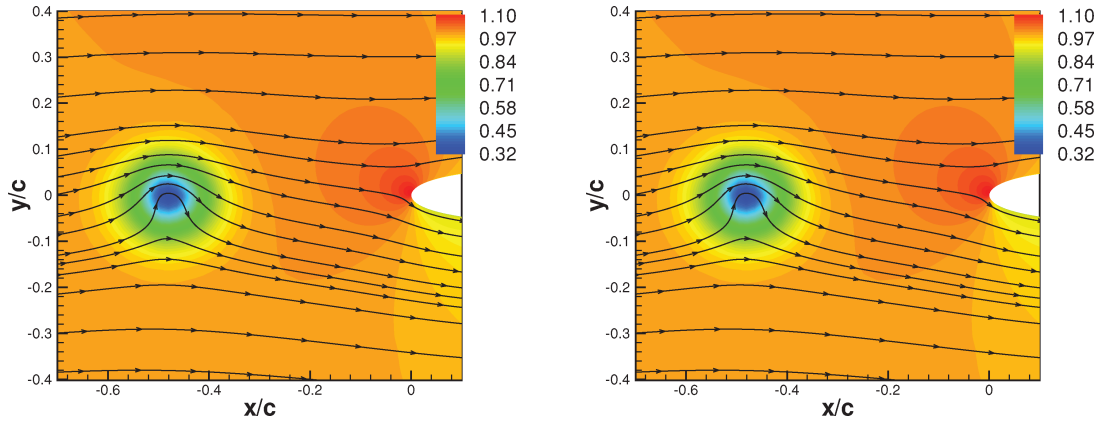

c) $\varepsilon = 1.6$: Inviscid

f) $\varepsilon = 1.6$: Viscous

Fig. 5 Effect of the ε parameter on the vortex path and on the size of the vortex core for inviscid (a, b, c) and viscous (d, e, f) calculations. Density contours are shown along with streamlines at the same instant $t(U_\infty/c) = 4.0$. The vortex was introduced 4.5 chords ahead of the airfoil. Note that the lowest value of density corresponds to the density at the vortex core.

reasonably predict the oscillation of stagnation point[28] and flow separation,[17] which determines the movement of the high-pressure region towards the low-pressure region near the LE of the airfoil.[15] As explained in Refs. 17, 28, and 29, a secondary vortex is formed beneath the airfoil as a result of the flow separation. The induced velocity of the clockwise-rotating vortex makes the stagnation point move up. Then the flow speed decreases on the upper surface and increases on the lower surface leading to the creation of a secondary anticlockwise vortex. The original and the secondary vortices get weakened after combining, and they separate more and more from the airfoil. This explains why their effects on the flow over the aft of the airfoil is minimal. The density contours are compared against the experiments by Lee and Bershader[15] in Fig. 9, and good agreement is obtained. Note that the small oscillation on the C_p curve, which occurs after the main interaction on the fine grid, is apparently caused by the scaling used for the ε parameter.

E. Influence of the Time Refinement

The vortex was introduced at 1.5 chords ahead of the airfoil, and calculations were carried out on the coarse grid of 125,000 points. It was found that the C_p values are very well predicted for the different time steps. Differences appear at the chordwise section $x/c = 0.05$,

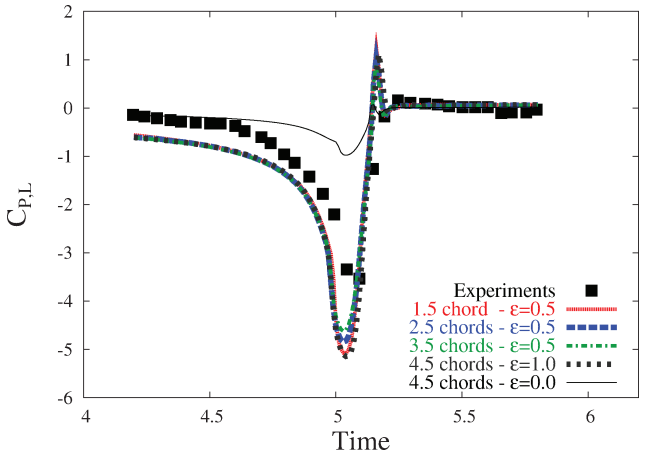

a) Lower surface, $x/c = 0.02$

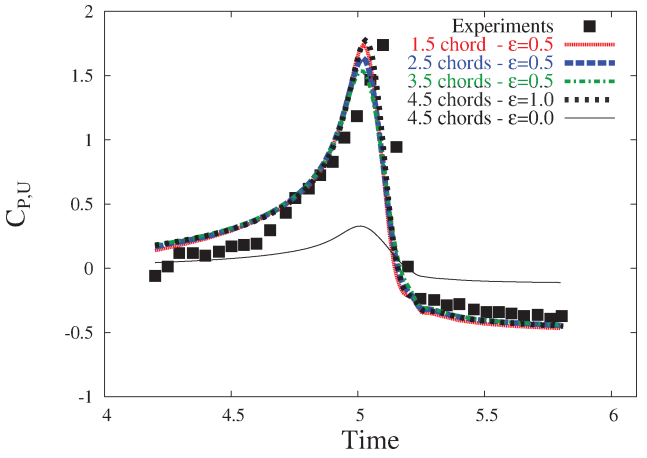

b) Upper surface, $x/c = 0.02$

Fig. 6 Influence of the initial vortex location on the time history of the surface-pressure coefficient. Head-on BVI problem, NACA-0012 airfoil, inviscid calculation, Mach number 0.5, $x/c = 0.02$.

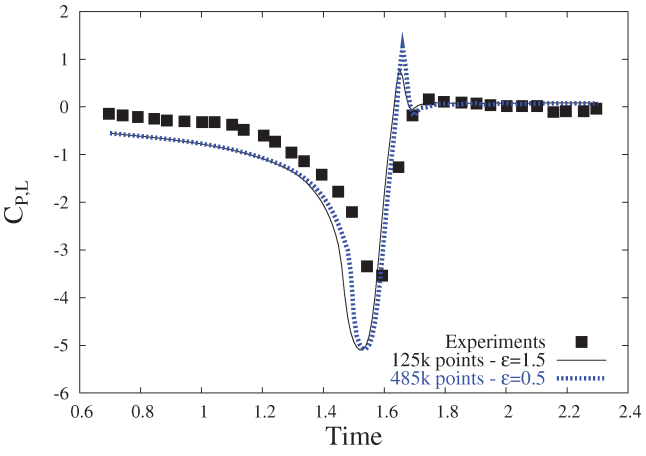

a) Lower surface, $x/c = 0.02$

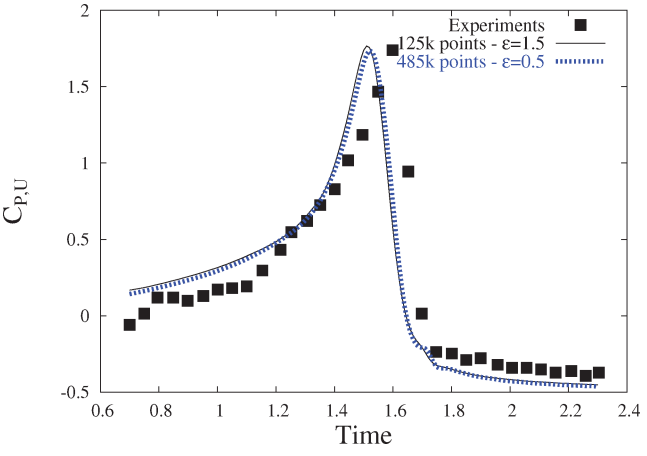

b) Upper surface, $x/c = 0.02$

Fig. 7 Influence of the spatial refinement on the time history of the surface-pressure coefficient. Head-on BVI problem, NACA-0012 airfoil, inviscid calculation, Mach number 0.5, $x/c = 0.02$.

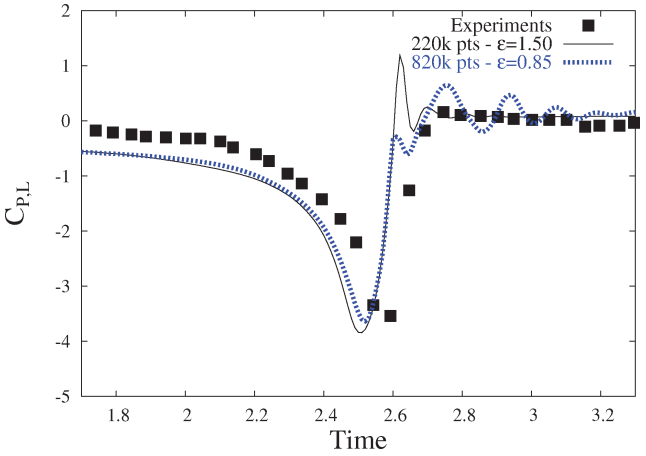

a) Lower surface, $x/c = 0.02$

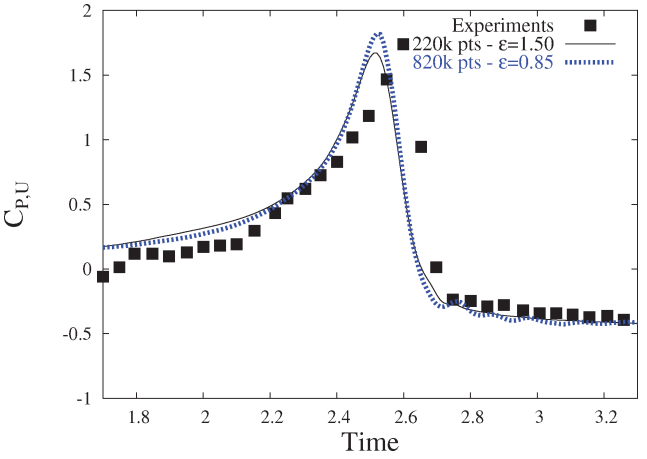

b) Upper surface, $x/c = 0.02$

Fig. 8 Influence of the spatial refinement on the time history of the surface-pressure coefficient. Head-on BVI problem, NACA-0012 airfoil, viscous calculation, Mach number 0.5, $x/c = 0.02$.

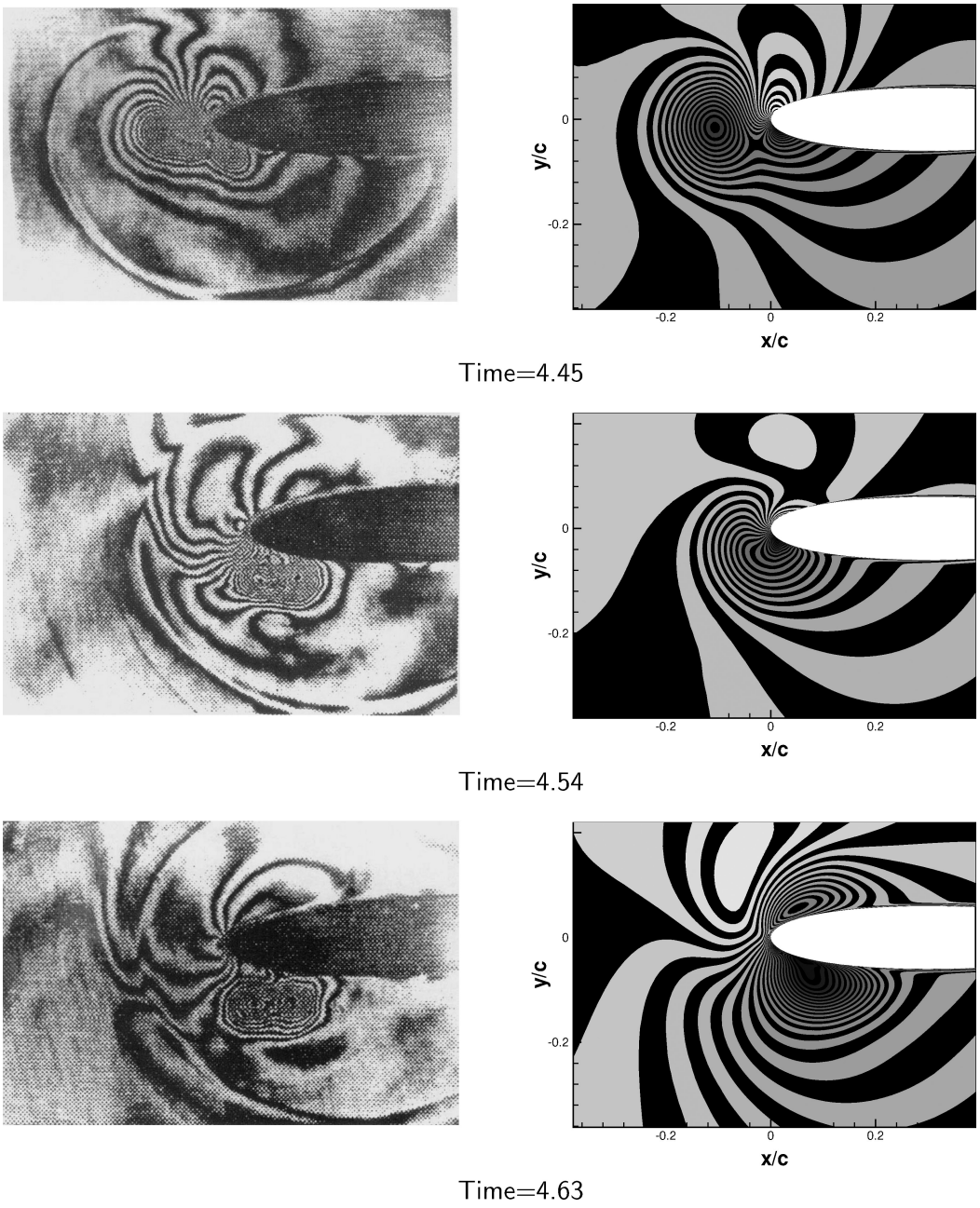

Fig. 9 Comparison between experimental holographic interferograms (by Lee and Bershader[15]) and computational density contours for the head-on BVI case. The vortex was introduced 4.5 chords ahead of the airfoil, and the calculations were performed using the k–ω model. The time step Δt is nondimensionalized with the freestream velocity U_∞ and the airfoil chord c.

which is unlikely to affect the acoustical pressure because the main interaction near the LE is well predicted.

Viscous calculations were run using the k–ω and shear stress transport (SST) models for two different time steps 0.01 and 0.001 with the vortex being introduced at 2.5 chords ahead of the airfoil. The time refinement was found to modify the strength of the secondary vortex, and again the viscous results were found to be more sensitive to the time refinement. The main acoustical wave was captured in a similar way for both turbulence models; which seems to indicate that a dimensionless time step of 0.01 is sufficient to get an estimation of the sound-pressure level (SPL) for this test case.

F. Influence of the Angles of Attack

It is noticeable (see Fig. 6a) that the computed surface C_p does not match the experiments before the interaction as if an angle of attack were present. It was suggested[30] that the clockwise-rotating vortices decrease locally the apparent angle of attack when passing below the airfoil, that is, they unload the blade. Therefore two viscous calculations with angles of attack 0.5 and 0.75 deg were carried out. The k–ω model was used, and the vortex was introduced at 2.5 chords ahead of the airfoil. Not only the presence of a small angle of attack gives a better match against the experiments regarding the C_p history before the interaction, but it also gives weaker C_p values at sections $x/c = 0.05$ and 0.10, as illustrated by Fig. 10.

Regarding the C_p value for $x/c = 0.02$, the interaction appears stronger for zero angle of attack because of the vortex path. After the vortex breakup, a larger part of the vortex propagates on the lower side of the airfoil (Fig. 11), explaining why the anticlockwise rotating secondary vortex is stronger in the case of zero angle of attack.

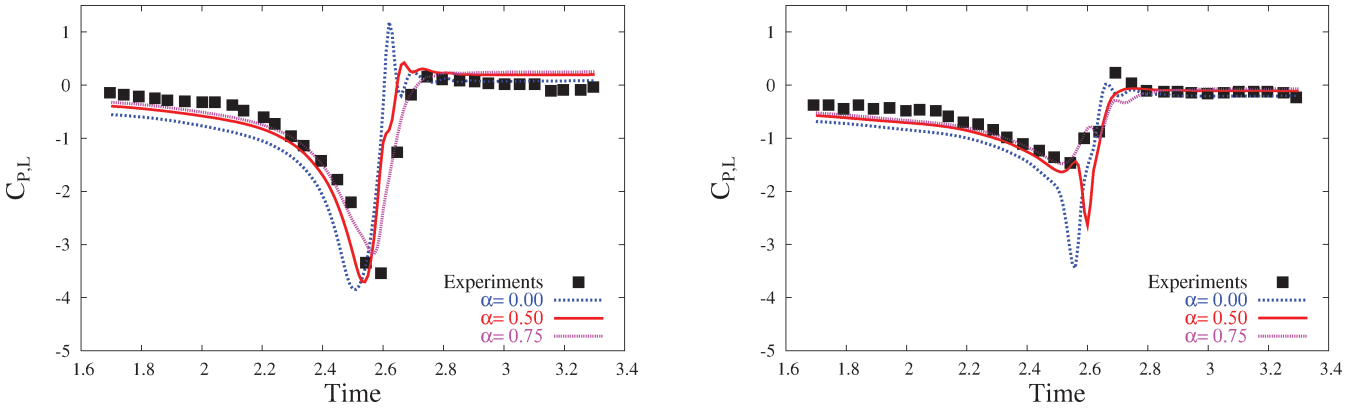

a) Lower surface, $x/c = 0.02$ **b) Lower surface, $x/c = 0.05$**

Fig. 10 Influence of the angle of attack on the time history of the surface-pressure coefficient. Head-on BVI problem, NACA-0012 airfoil, viscous calculation, Mach number 0.5: a) $x/c = 0.02$ and b) $x/c = 0.05$.

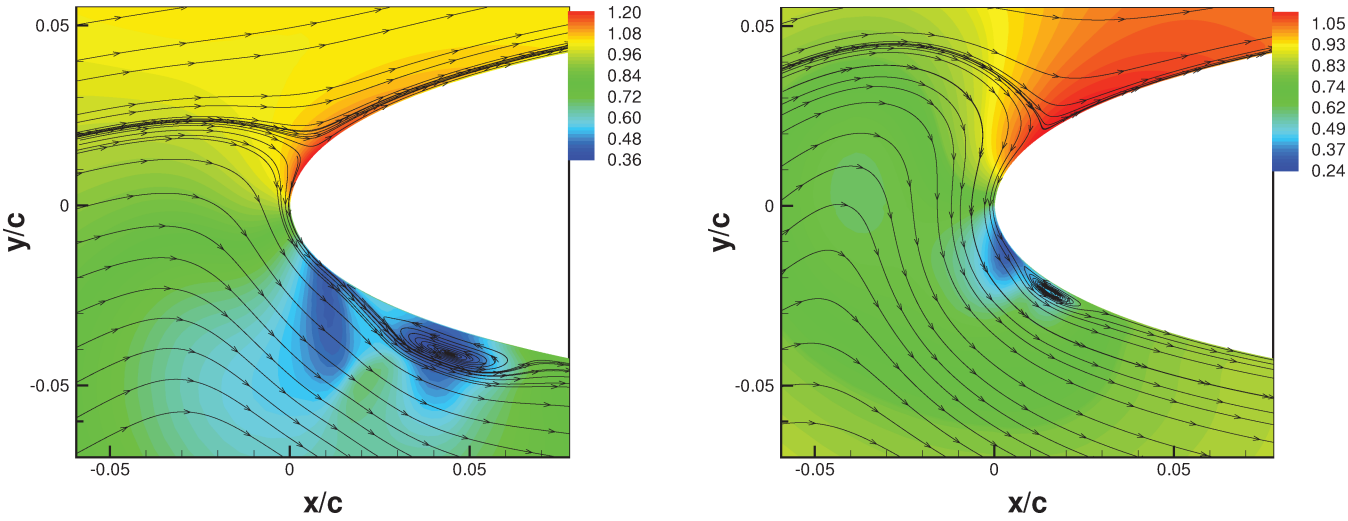

a) $\alpha = 0.00$, $t = 2.55$ **b) $\alpha = 0.75$, $t = 2.55$**

Fig. 11 Effect of the angle of attack on the location of the stagnation point. Density contours are shown along with streamlines at the same time instant.

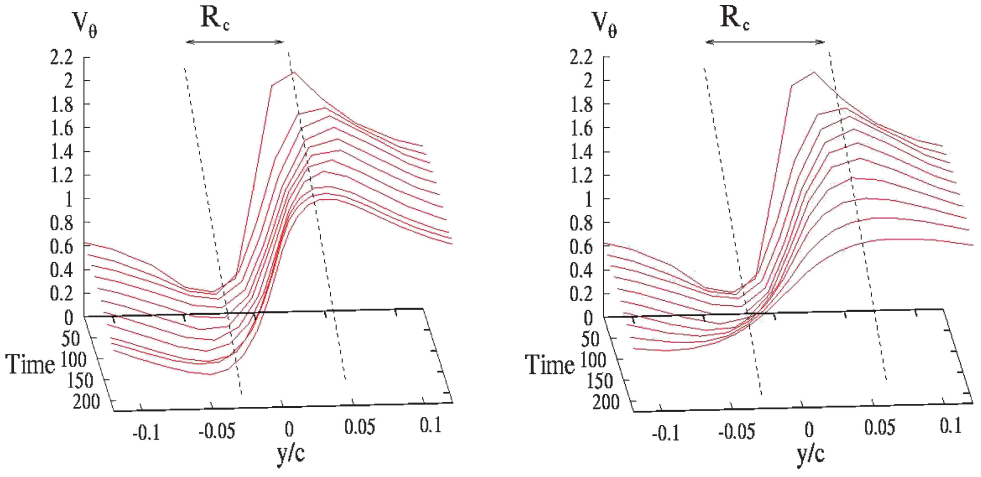

a) k–ω model **b) SST model**

Fig. 12 History of the tangential velocity profile along a vertical plane passing by the vortex core for the k–ω and the SST models. The vortex was introduced at 2.5 chords ahead of the airfoil. Head-on BVI problem, NACA-0012 airfoil, Mach number 0.5.

G. Influence of the Turbulence Models

Five different turbulence models have been tested: Spalart–Allmaras[31] (one-equation model), k–ω (Ref. 32), Pk limiter, Menter's baseline,[33] and Menter's shear stress transport[34] (two-equation models). The Pk limiter model[35] is a version of the k–ω model, which uses a limiter for the turbulence kinetic energy to reduce the eddy viscosity at the vortex cores.

To the knowledge of the authors, this is the first time that such a variety of turbulence models have been employed with the use of the CVCM. First, a comparison between the results given by the turbulence models gives some interesting features when the CVCM is applied. It was found that the CVCM is very sensitive to the value of ε for viscous calculations and that using a higher value than the optimum one did not increase proportionally the strength of the vortex, as found for inviscid calculations. This stems from the fact that the turbulence models generate eddy viscosity depending on the velocity gradients of the flow. The use of too high a value for ε can amplify the strength of the vortex. This will result in higher eddy viscosity, and consequently the initial vortex will be deformed, leading to a weaker interaction. As shown in Fig. 12, the deformation of the vortex varies with the turbulence model. Because the SST model produces less eddy viscosity, the size of the vortex increases. The peaks of surface-pressure coefficient are not of the same magnitude when the vortex is introduced at different vortex locations for a fixed ε parameter. For this test case, the optimum value of ε is set to 1.5 as for the inviscid calculations.

The turbulent Reynolds number, which is the ratio of turbulent eddy viscosity to molecular viscosity, gives an indication of the amount of turbulence generated by the model. It was observed that the baseline model behaves more like the k–ω model just before the CVCM is switched off at $t = 2.40$, the Pk limiter and the SST remaining similar. As depicted in Fig. 13, the k–ω model produces more eddy viscosity at the vortex core than the SST model, and the one-equation SA model has a very diffused Re_T field.

To compare the turbulence models during the interaction, no confinement was applied within a distance 0.1 chord from the airfoil. The C_p history is given in Fig. 14 for the different turbulence models. On the suction side of the airfoil, the magnitude of the peaks is similar for all of the models but the SST, which gives a lower value especially at the chordwise section $x/c = 0.02$. The magnitude of the pressure coefficients given by the other models, and the inviscid calculations, are comparable indicating that the viscous effects are not important on the upper side of the airfoil. On the pressure side, a similar behavior is observed for the baseline, k–ω, and one-equation models, which produce similar levels of turbulence. The Pk limiter model was found to overpredict the strength of the secondary vortex. The secondary peaks are predicted by the viscous calculations because there is a transfer of energy between the original vortex and the boundary layer, explaining the higher pressure coefficient peak at $x = 0.02$ for the inviscid calculations. Therefore, the differences between the employed turbulence models are reflected in the obtained results, particularly on the lower side of the airfoil where the vortex interacts with the boundary layer.

H. Transonic Case

Results are now discussed for a transonic flow of a freestream Mach number of 0.8. The history of the surface-pressure coefficient is shown in Fig. 15. Despite the fact that the most pronounced interaction is observed when the vortex passes under the airfoil, at transonic flow, the peaks for the loads are lower. This is apparently because of the presence of shocks. The vortex, while moving over the surface of the airfoil encounters the shock, thickens the shock and regains some strength, explaining why the C_p bandwidth is larger. Regarding the history of the lift, it is interesting to establish a comparison between the subsonic and transonic flows (Fig. 16). The lift coefficient is observed to be negative when the vortex induces a downwash at the LE of the airfoil in both subsonic and transonic flows. Afterwards, when the vortex passes the LE the lift coefficient rapidly increases. The lift for the transonic flow is less

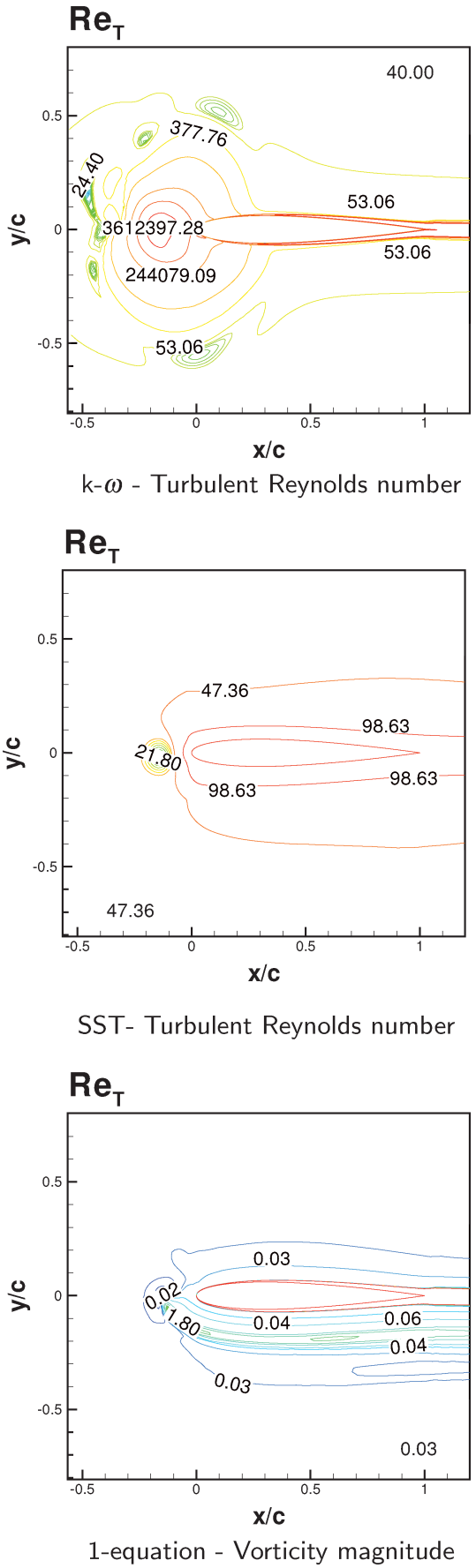

Fig. 13 Turbulent Reynolds number for different turbulence models; flow at a Mach number of 0.5 for $t = 2.40$.

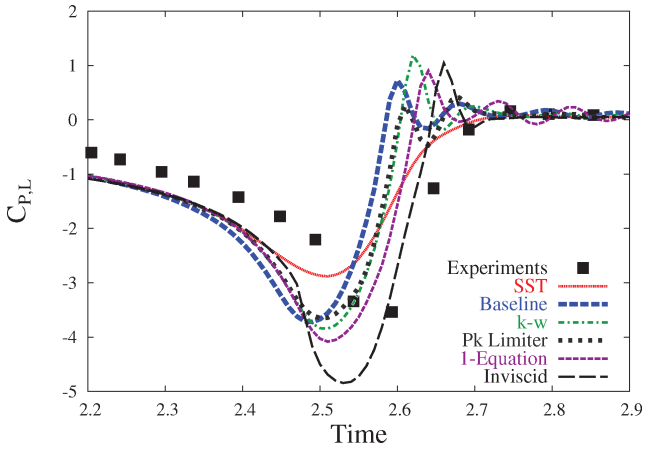

a) Lower surface, $x/c = 0.02$

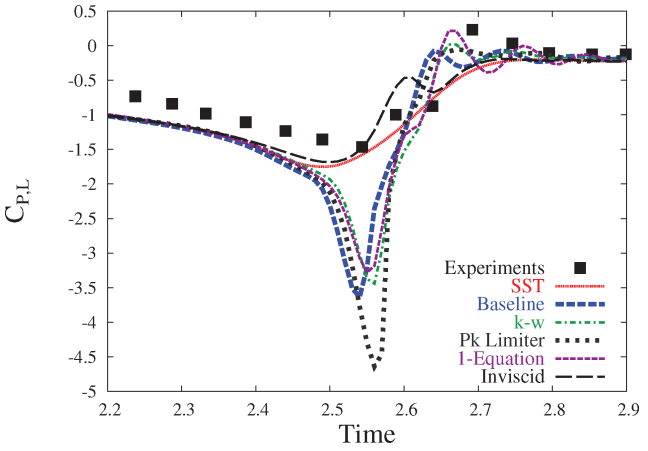

c) Lower surface, $x/c = 0.05$

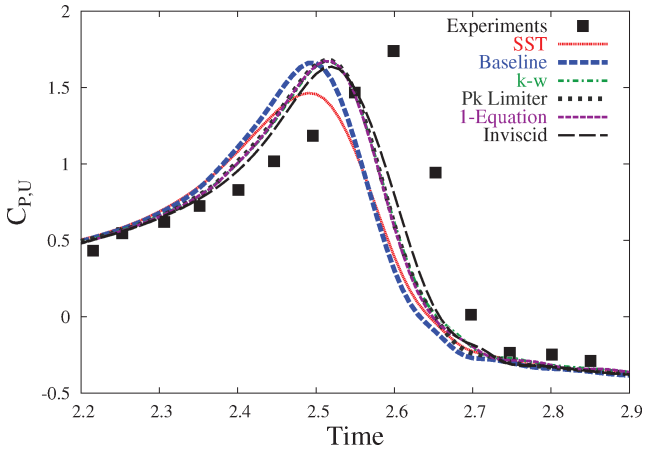

b) Upper surface, $x/c = 0.02$

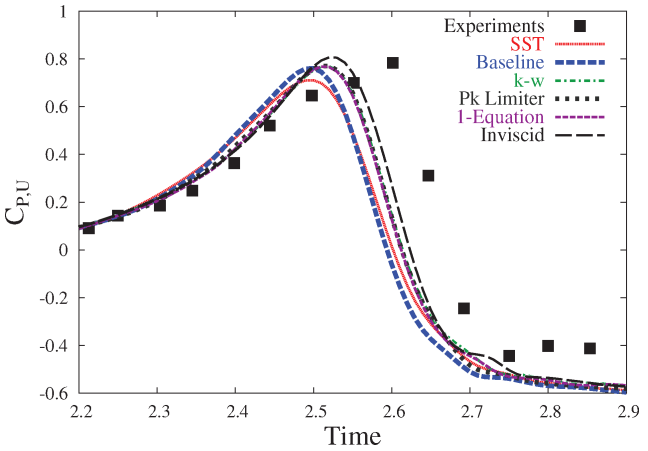

d) Upper surface, $x/c = 0.05$

Fig. 14 Time history of the surface-pressure coefficient obtained with various turbulence models. Head-on BVI problem, NACA-0012 airfoil, viscous calculation, Mach number 0.5.

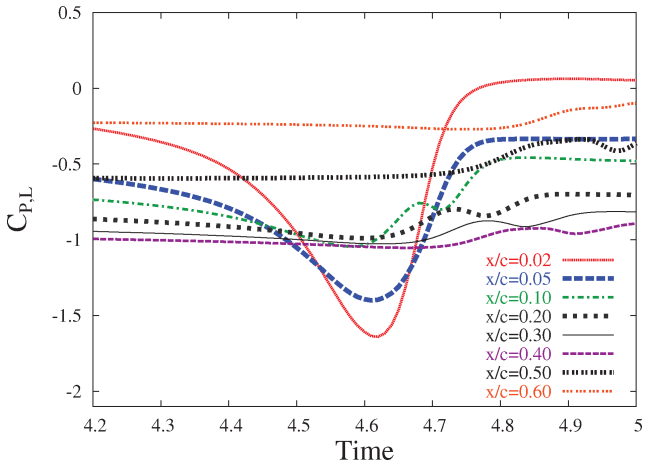

a) Lower surface

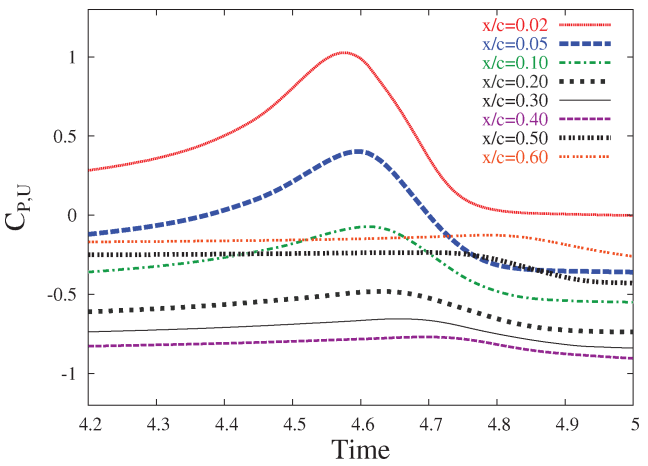

b) Upper surface

Fig. 15 Time history of the surface-pressure coefficient at different tap locations. Head-on BVI problem, NACA-0012 airfoil, viscous calculation, Mach number 0.8.

affected by the passage of the vortex, which is now weakened by the presence of the shock. For the transonic case, the same vortex properties as for the subsonic one have been used; unfortunately, no BVI experiments are available for higher Mach numbers.

V. Airfoil-Vortex Noise Simulation

So far the aerodynamics of the interaction, as characterized by the surface pressures, have been considered. The differences when considering acoustics are now discussed. The acoustical pressure that corresponds to the pressure fluctuations from the undisturbed medium is studied. This is given by $P'(\boldsymbol{x}, t) = P(\boldsymbol{x}, t) - \overline{P(\boldsymbol{x}, t)}$, where $P(\boldsymbol{x}, t)$ comes from the CFD solution and $\overline{P(\boldsymbol{x}, t)}$ is the time-averaged pressure. The first parameter to be checked for the calculations of the acoustical pressure was the vortex location. Although the pressure coefficient on the airfoil can be correctly predicted for the four different vortex locations (see Sec. IV.C), nonphysical waves appear. Indeed, at the first time steps the difficulties of the

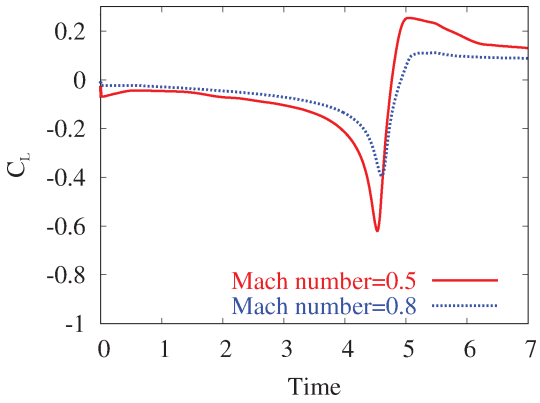

Fig. 16 History of the lift coefficient at Mach numbers of 0.5 and 0.8 for the NACA-0012 airfoil.

solver in perfectly assimilating the vortex into the flow solution are manifested by the creation of spurious waves that start to propagate from the airfoil. The acoustical analysis is spoiled by the presence of these waves and necessitates the vortex to be introduced at least 4.5 chords ahead of the airfoil.

The same head-on BVI has been simulated for the NACA-0012 for subsonic and transonic flow conditions. The C_p history and the acoustical pressure of the vortex-airfoil interaction are presented in the next sections. It will be shown that the BVI noise is determined by three mechanisms of aerodynamic sound generation: the compressibility waves, the transonic waves,[20] and the trailing-edge noise.[27]

A. High Subsonic Flow

The high directivity of BVI noise is usually illustrated by two distinct radiation lobes. These two waves are called compressibility waves, which are typical for high subsonic flow at the vortex break-up.[36,37] The presence of the vortex causes the unsteady displacement of the stagnation point of the flow at the LE of the airfoil. Then an enlarged high-pressure region is generated and then propagates upstream as for steepening shock waves.[38] The two waves, which are denoted by A and B in Fig. 17a are generated below and above the airfoil. Once these waves have reached the trailing edge, other waves start to form and propagate upstream resulting in trailing-edge noise. The trailing-edge waves are depicted by C and D.

Placing a probe at point P (see Fig. 17a) and plotting the trace of SPL, which is defined as $20\ \log_{10}[P'(\boldsymbol{x}, t)/2e-5)]$, one reveals the passage of the acoustical wave A. The effect of this wave on the SPL is the peak shown in Fig. 17b at time $t(U_\infty/c) = 5$.

B. Transonic Flow

An additional acoustical wave to the compressibility and the trailing-edge ones is present for transonic flow. This wave, called the transonic wave, emerges when a supersonic flow region is generated along the shoulder of the airfoil.[38] As explained in Refs. 20 and 26, a shock wave appears after the vortex reaches the maximum thickness of the airfoil beyond which the supersonic area collapses. Then the shock wave moves upstream leaving the LE in a downward direction while the stagnation point moves upward. This results in the generation of a sound wave propagating upstream.[37] The acoustical pressure and the Mach-number contours for two instances are given in Fig. 18 with the acoustical wave denoted by E. As expected, the compressibility and trailing-edge waves are also present for the transonic flow case (see Figs. 18a and 18b). There are significant differences in the strength and direction of the acoustical waves between the two Mach numbers. Despite the fact that the passage of the vortex does not perturb the loads of the airfoil as much in the transonic case, the level of acoustical pressure is higher than for the subsonic case. The directivity patterns of the noise are different as a result of the presence of the shocks that modify the trajectory of the acoustical waves. It takes more time for the acoustical waves to

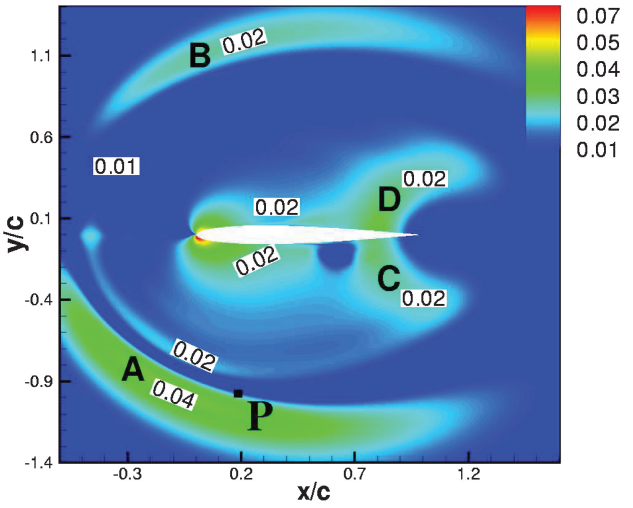

Fig. 17a Absolute value of the acoustical pressure at $t(U_\infty/c) = 5.10$ and Mach number of 0.5. The acoustical pressure is nondimensionalized against the freestream pressure.

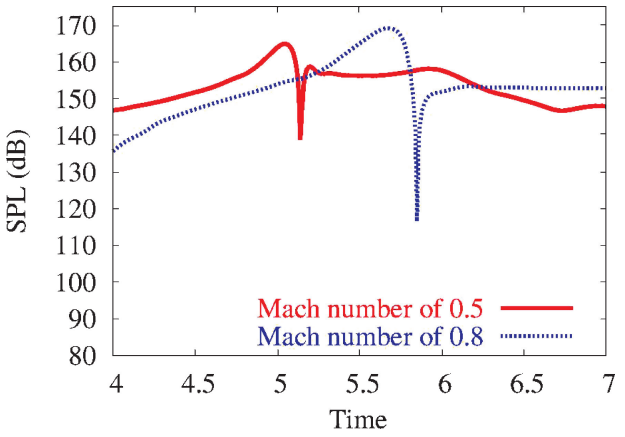

Fig. 17b Sound pressure level history at point P.

be generated for the transonic case than for the subsonic one (see Fig. 17b).

It is interesting to observe the time evolution of the acoustical pressure at different locations. As shown in Fig. 19, the acoustical signal dissipates rapidly. Despite the fact that the CVCM is capable of conserving vorticity, the present formulation cannot preserve the acoustical waves, which tend to dissipate in most CFD solvers. This implies that only the near-field close to the airfoil is correctly captured by CFD and hence can be used as input data for computational aeroacoustics. A very fine grid or/and the adoption of a high-order spatial scheme would allow the preservation of the acoustical waves for longer.

Two different approaches are known for determining the far-field noise: the Kirchhoff method[39] and the Ffowcs Williams–Hawkings method (FW-H) (see Refs. 40 and 41). Both aeroacoustical methods require the near-field acoustics to be supplied by the CFD solution. As mentioned by Brentner and Farassat,[42] the Kirchhoff method requires the use of a near field, which is usually distant by at least one chord from the airfoil to include the nonlinear effects of the flow on the acoustics, which would make the Kirchhoff method unreliable for our case because of the attenuation of the pressure waves. Nevertheless, the determination of the far-field noise remains possible with the use of the FW-H method, which only needs the C_p history or the very close near-field acoustics. Because the loads history can be well predicted with the use of the CVCM, the FW-H will be preferred for a future study of the far-field noise for the cases presented in this paper. As in most acoustic codes based on the FW-H formulation, our approach will consider the linear thickness and loading terms of the FW-H equation, neglecting the nonlinear quadrupole term.

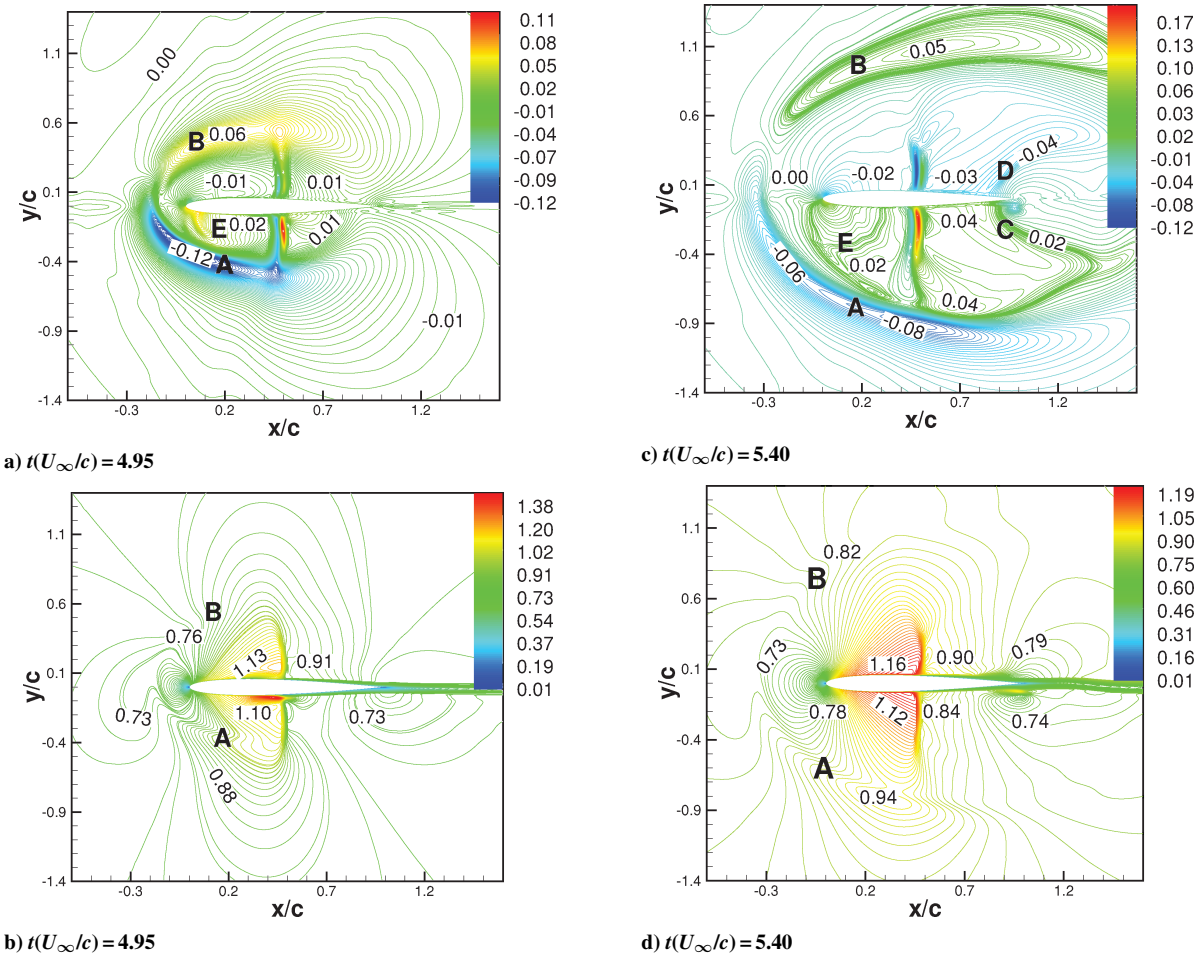

Fig. 18 Two different instants for (a, c) acoustical pressure and (b, d) Mach-number contours. NACA-0012 airfoil, head-on BVI case. The freestream Mach number is 0.8. Note that the acoustical pressure is nondimensionalized using the freestream dynamic pressure.

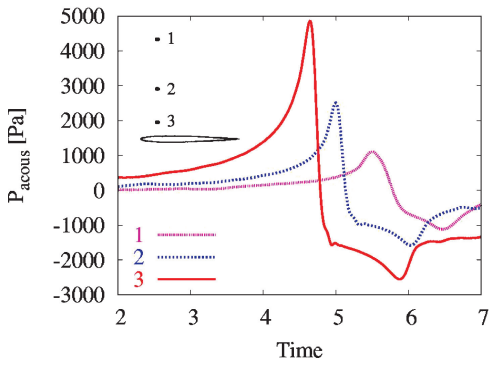

Fig. 19a Acoustic pressure history at points 1, 2, 3 above the airfoil.

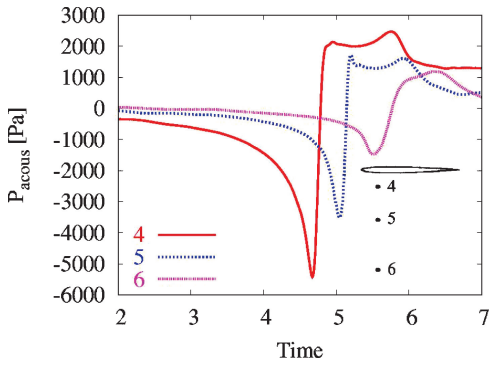

Fig. 19b Acoustic pressure history at points 4, 5, 6 below the airfoil. Head-on BVI problem, NACA-0012 airfoil, viscous calculations, Mach number 0.5.

VI. Conclusions

Present results indicate that accurate predictions of blade-vortex interaction (BVI) can be obtained using the compressible vorticity confinement method (CVCM). First indications reveal that the predictions are not so sensitive to the parameters of the method considering that different grids with the appropriate epsilon give similar results. The CVCM made possible the simulation of BVI using an existing computational-fluid-dynamics (CFD) code and the overhead in terms of CPU time and memory was minimal. Further investigation is needed to make the method as independent as possible from the value of the confinement parameter, that could be possibly achieved by taking into account the properties of the spatial discretisation scheme.

The present calculations demonstrate that accurate prediction of the surface-pressure coefficient is possible for head-on BVI cases. The predicted acoustic field is in qualitative agreement with experimental observations at subsonic and transonic flow conditions. However, additional validation cases are necessary to improve the fidelity of the CFD results. Direct comparison between acoustic measurements and CFD would be beneficial, and this could reveal further limitations stemming from the order of the employed numerical scheme.

Acknowledgments

This work was supported by Westland Helicopters, Limited. The authors thank M. Costes and J. Ballmann, as well as the anonymous reviewers for their constructive comments on this work.

References

[1]Booth, E. R., Jr., "Experimental Observations of Two-Dimensional Blade-Vortex Interaction," *AIAA Journal*, Vol. 28, No. 8, 1990, pp. 1353–1359.

[2]Schmitz, F. H., Gopalan, G., and Sim, B. W.-C., "Flight Path Management and Control Methodology to Reduce Helicopter Blade-Vortex Interaction (BVI) Noise," *Journal of Aircraft*, Vol. 39, No. 2, 2002, pp. 193–205.

[3]Leverton, J. W., "25 Years of Rotorcraft Aeroacoustics: Historical Perspective and Important Issue," *Journal of Sound and Vibration*, Vol. 133, No. 2, 1989, pp. 261–287.

[4]Schmitz, F. H., and Yu, Y. H., "Helicopter Impulsive Noise: Theoretical and Experimental Status," *Journal of Sound and Vibration*, Vol. 109, No. 3, 1986, pp. 361–422.

[5]Badcock, K. J., and Richards, B. E., "Implicit Time-Stepping Methods for the Navier–Stokes Equations,"*AIAA Journal*, Vol. 34, No. 3, 1996, pp. 555–559.

[6]Steinhoff, J., and Raviprakash, G. K.,"Navier–Stokes Computation of Blade-Vortex Interaction Using Vorticity Confinement," AIAA Paper 95-0161, Jan. 1995.

[7]Steinhoff, J., Wenren, Y., Wang, L., Fan, M., Xiao, M., and Braun, C., "The Computation of Flow over Helicopter Rotors and Complex Bodies Using Vorticity Confinement," Univ. of Space Inst., Tech. Rept., TN 37388, Tullahoma, TN, 2001, pp. 699–707.

[8]Steinhoff, J., and Underhill, D., "Modification of the Euler Equations for Vorticity Confinement: Application to the Computation of Interacting Vortex Rings," *Journal of Physics Fluid*, Vol. 6, No. 8, 1994, pp. 2738–2744.

[9]Lönher, R., and Yang, C., "Tracking Vortices over Large Distances Using Vorticity Confinement," European Community on Computational Methods in Applied Sciences (ECCOMAS) CFD 2001, Sept. 2001.

[10]Murayama, M., Nakahashi, K., and Obayashi, S., "Numerical Simulation of Vortical Flows Using Vorticity Confinement Coupled with Unstructured Grid," AIAA Paper 2001-0606, Jan. 2001.

[11]Weren, Y., Fan, M., Dietz, W., Hu, G., Braun, C., Steinhoff, J., and Grossman, B.,"Efficient Eulerian Computation of Realistic Rotorcraft Flows Using Vorticity Confinement," AIAA Paper 2001-0996, Jan. 2001.

[12]Dietz, W., Fan, M., Steinhoff, J., and Wenren, Y., "Application of Vorticity Confinement to the Prediction of the Flow over Complex Bodies," AIAA Paper 2001-2642, June 2001.

[13]Hu, G., and Grossman, B., "The Computation of Massively Separated Flows Using Compressible Vorticity Confinement Methods," AIAA Paper 2002-0136, Jan. 2002.

[14]Fedkiw, R., Stam, J., and Jensen, H. W., "Visual Simulation of Smoke," *SIGGRAPH 2001 Conference Proceedings*, Annual Conf. Series, Assoc. Computing Machinery, New York, 2001, pp. 15–22.

[15]Lee, S., and Bershader, D., "Head-On Parallel Blade-Vortex Interaction," *AIAA Journal*, Vol. 32, No. 1, 1994, pp. 16–22.

[16]Lee, S., and Bershader, D., "An Experimental and Computational Study of 2-D Parallel Blade-Vortex Interaction," AIAA Paper 91-3277, Sept. 1991.

[17]Ng, N., and Hillier, R., "Numerical Investigation of the Transonic Blade-Vortex Interaction," AIAA Paper 97-1846, June–July 1997.

[18]Oh, W. S., Kim, J. S., and Kwon, O. J., "An Unstructured Dynamic Mesh Procedure for 2-D Unsteady Viscous Flow Simulations," AIAA Paper 2002-0121, Jan. 2002.

[19]Oh, W. S., Kim, J. S., and Kwon, O. J., "Numerical Simulation of Two-Dimensional Blade-Vortex Interactions Using Unstructured Adaptive Meshes," *AIAA Journal*, Vol. 40, No. 3, 2002, pp. 474–480.

[20]Lent, H.-M., Meier, G. E. A., Muller, K. J., Obermeier, F., Schievelbusch, U., and Shurmann, O., "Mechanisms of Transonic Blade-Vortex Interaction Noise," *Journal of Aircraft*, Vol. 30, No. 1, 1993, pp. 88–93.

[21]Hu, G., and Grossman, B., "Numerical Method for Vorticity Confinement in Compressible Flow," *AIAA Journal*, Vol. 40, No. 10, 2002, pp. 1945–1953.

[22]Hu, G., "The Development and Applications of a Numerical Method for Compressible Vorticity Confinement in Vortex-Dominant Flows," Ph.D. Dissertation, Dept. of Aerospace and Ocean Engineering, Virginia Polytechnic Inst. and State Univ., Blacksburg, VA, June 2001.

[23]Costes, M., and Kowani, G., "An Automatic Anti-Diffusion Method for Vortical Flows Based on Vorticity Confinement," *Aerospace Science and Technology*, Vol. 7, No. 1, 2003, pp. 11–21.

[24]Fan, M., Weren, Y., Dietz, W., Xiao, M., and Steinhoff, J., "Computing Blunt Body Flows on Coarse Grids Using Vorticity Confinement," *Journal of Fluids Engineering*, Vol. 124, No. 4, 2002, pp. 876–885.

[25]Wenren, Y., Fan, M., Wang, L., Xiao, M., and Steinhoff, J., "Application of Vorticity Confinement to the Prediction of the Flow over Complex Bodies," *AIAA Journal*, Vol. 41, No. 5, 2003, pp. 809–815.

[26]Körber, S., and Ballmann, J., "Mechanisms and Acoustics of Blade-Vortex-Interactions," *Zeitschniff fur Flugwissenschoften, Weltraumforsh*, Vol. 19, 1995, pp. 397–406.

[27]Hardin, J. C., and Lamkin, S. L., "Aeroacoustic Interaction of a Distributed Vortex with a Lifting Joukowski Airfoil," AIAA Paper 84-2287, Oct. 1984.

[28]Tung, C., and Yu, Y. H., "Aerodynamic Aspects of Blade-Vortex Interaction (BVI)," AIAA Paper 96-2010, June 1996.

[29]Mandella, M., and Bershader, D., "Quantitative Study of the Compressible Vortex: Generation, Structure and Interaction with Airfoils," AIAA Paper 87-0328, Jan. 1987.

[30]Wilder, M. C., and Telionis, D. P., "Parallel Blade-Vortex Interaction," *Journal of Fluids and Structures*, Vol. 12, No. 7, 1998, pp. 801–838.

[31]Spalart, P. R., and Allmaras, S. R., "A One-Equation Turbulence Model for Aerodynamic Flows," *La Recherche Aérospatiale*, Vol. 1, 1994, pp. 5–21.

[32]Wilcox, D. C., Turbulence Modelling for CFD, DCW Industries, Inc., La Canada, CA, 1993.

[33]Menter, F. R., "Two-Equation Eddy-Viscosity Turbulence Models for Engineering Applications," *AIAA Journal*, Vol. 32, No. 8, 1994, pp. 1598–1605.

[34]Menter, F. R., "Zonal Two-Equation k–ω Turbulence Models for Aerodynamic Flows," AIAA Paper 93-2906, July 1993.

[35]Brandsma, F. J., Kok, J. C., Dol, H. S., and Elsenaar, A., "Leading-Edge Vortex Flow Computations and Comparison with DNW-HST Wind Tunnel Data," RTO/AVT Vortex Flow Symposium, 2001.

[36]Yu, Y. H., "Rotor Blade-Vortex Interaction Noise," *Progress in Aerospace Sciences*, Vol. 36, No. 2, 2000, pp. 97–115.

[37]Kaminski, W. S., and Szumowski, A. P., "Acoustic Effects of Parallel Vortex-Airfoil Interaction," *Journal of Sound and Vibration*, Vol. 183, No. 2, 1995, pp. 209–220.

[38]Ellzey, J. L., and Henneke, M. R., "The Acoustic Wave from a Shock-Vortex Interaction: Comparison Between Theory and Computation," *Fluid Dynamics Research*, Vol. 27, No. 1, 2000, pp. 53–64.

[39]Farassat, F., "Generalized Functions and Kirchhoff Formulas," AIAA Paper 96-1705, May 1996.

[40]Farassat, F., "Theory of Noise Generation from Moving Bodies with an Application to Helicopter Rotors," NASA TR R-451, Dec. 1975.

[41]Long, L. N., Souliez, F., and Sharma, A., "Aerodynamic Noise Prediction Using Parallel Methods on Unstructured Grids," AIAA Paper 2001-2196, May 2001.

[42]Brentner, K. S., and Farassat, F., "Modeling Aerodynamically Generated Sound of Helicopter Rotors," *Progress in Aerospace Sciences*, Vol. 39, Nos. 2–3, 2003, pp. 83–120.

H. Atassi
Associate Editor